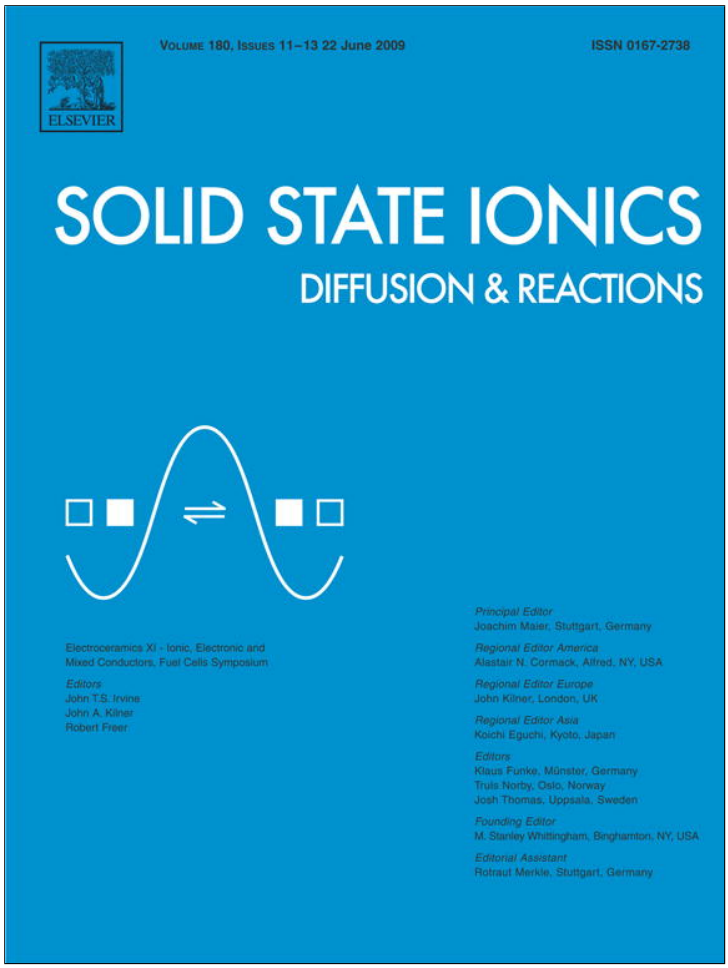

Solid State Ionics 180 (2009) 878–885

Contents lists available at ScienceDirect

Solid State Ionics

journal homepage: www.elsevier.com/locate/ssi

Performance of perovskite-related oxide cathodes in contact with lanthanum silicate electrolyte

A.A. Yaremchenko [a,*], V.V. Kharton [a], D.O. Bannikov [a,b], D.V. Znosak [a], J.R. Frade [a], V.A. Cherepanov [b]

[a] Department of Ceramics and Glass Engineering, CICECO, University of Aveiro, 3810-193 Aveiro, Portugal
[b] Department of Chemistry, Ural State University, Lenin av. 51, Ekaterinburg 620083, Russia

ARTICLE INFO

Article history:
Received 10 September 2008
Received in revised form 8 January 2009
Accepted 2 February 2009

Keywords:
Solid oxide fuel cell cathode
Mixed conductor
Perovskite
Ruddlesden–Popper nickelate
Apatite-type solid electrolyte
Electrode polarization
Silicate

ABSTRACT

The cathodic performance of selected mixed-conducting electrodes, including perovskite-type $SrMn_{0.6}Nb_{0.4}O_{3-\delta}$, $Sr_{0.7}Ce_{0.3}Mn_{0.9}Cr_{0.1}O_{3-\delta}$ and $Gd_{0.6}Ca_{0.4}Mn_{0.9}Ni_{0.1}O_{3-\delta}$, and Ruddlesden–Popper $La_2Ni_{0.5}Cu_{0.5}O_{4+\delta}$, $LaSr_2Mn_{1.6}Ni_{0.4}O_{7-\delta}$, $La_4Ni_{3-x}Cu_xO_{10-\delta}$ ($x=0$–0.1) and $La_{3.95}Sr_{0.05}Ni_2CoO_{10-\delta}$, was evaluated in contact with apatite-type $La_{10}Si_5AlO_{26.5}$ solid electrolyte at 873–1073 K and atmospheric oxygen pressure. The electrochemical activity of porous nickelate-based layers was found to correlate with the concentration of mobile ionic charge carriers and bulk oxygen transport, thus lowering in the series $La_4Ni_{2.9}Cu_{0.1}O_{10-\delta} > La_4Ni_3O_{10-\delta} > La_{3.95}Sr_{0.05}Ni_2CoO_{10-\delta}$ and decreasing on copper doping in K_2NiF_4-type $La_2Ni_{1-x}Cu_xO_{4-\delta}$. The relatively high overpotentials of nickelate-based cathodes, varying in the range −240 to −370 mV at 1073 K and current density of −200 mA/cm^2, are primarily associated with surface diffusion of silica from $La_{10}Si_5AlO_{26.5}$, which partially blocks the electrochemical reaction zone. As compared to the intergrowth nickelate materials, the manganite-based electrodes exhibit substantially worse electrochemical properties, in correlation with the level of oxygen-ionic and electronic conduction in Mn-containing phases. The effects of cation interdiffusion between the cell components as a performance-deteriorating factor are briefly discussed.

1. Introduction

Apatite-type $La_{10-x}(SiO_4)_6O_{2\pm\delta}$ silicates possess a substantially high oxygen-ionic conductivity, moderate thermal expansion, low electronic transport in a wide range of oxygen chemical potentials and relatively low costs, and may thus be considered for potential use as solid oxide fuel cells (SOFCs) electrolytes [1–7]. The ionic conduction in these phases is dominated by interstitial migration mechanism and increases with oxygen content, which can be optimized by aliovalent doping and/or by the creation of lanthanum vacancies. Also, partial substitution of Si^{4+} makes it possible to suppress volatilization of silicon oxide from the apatite ceramics surface layers responsible for the electrolyte degradation under reducing conditions [6]. The maximum ionic transport in $La_{10-x}Si_{6-y}Al_yO_{27-\delta}$ ($x=0$–0.33, $y=0.5$–1.5) system is observed for the compositions close to $La_{10}Si_5AlO_{26.5}$ [6]. In the intermediate-temperature range important for SOFC operation, 800–1000 K, the conductivity of the latter composition is higher than that of yttria-stabilized zirconia.

The information on electrochemical behavior of various electrode materials in contact with apatite-type solid electrolytes is, however, very scarce. The number of cathode materials, thermomechanically compatible with lanthanum silicate-based ceramics, is essentially limited to perovskite-related phases with moderate thermal expansion, such as manganite-, nickelate- and cuprate-based systems [7]. State-of-the-art cathodes based on perovskite-type $(La,Sr)MnO_{3-\delta}$ (LSM) exhibit a poor oxygen-ionic conductivity and insufficient electrocatalytic activity in the intermediate temperature range [8,9]. In framework of the comparative assessment of alternative electrode materials, several Mn-containing phases with the ABO_3 perovskite structure were tested in this work. As decreasing A-site cation radius in the manganite lattice and modest doping by the lower-valence transition metal cations have often positive effects on the cathode properties [9,10], perovskite-type $Gd_{0.6}Ca_{0.4}Mn_{0.9}Ni_{0.1}O_{3-\delta}$ was selected as one model composition. Two other model materials, $Sr_{0.7}Ce_{0.3}Mn_{0.9}Cr_{0.1}O_{3-\delta}$ and $SrMn_{0.6}Nb_{0.4}O_{3-\delta}$, are the derivatives of $(Sr,Ce)MnO_{3-\delta}$ and $Sr(Mn,Nb)O_{3-\delta}$ solid solutions considered for potential use in the SOFC electrodes [11–13]; Ce-substituted strontium manganite possesses, in particular, better ionic and electronic transport properties compared to the well-known $(La,Sr)MnO_{3-\delta}$ series [11,12]. The available data on the electrochemical properties of $SrMnO_{3-\delta}$-based compounds are however limited. Another promising family of the intermediate-temperature SOFC cathode materials relates to Ruddlesden–Popper (RP) phases with general formula $A_{n+1}B_nO_{3n+1}$ and $n=1$–3, containing nickel in the B sites [9,14–19]. For example, attractively low cathodic overpotentials were reported for $La_2Ni_{0.8}Cu_{0.2}O_{4+\delta}$ electrode applied onto lanthanum silicate-based solid electrolyte [16]. In order to further explore the potential of intergrowth nickelates for the SOFC cathodes, the following compositions were selected: $La_2Ni_{0.5}Cu_{0.5}O_{4+\delta}$, $La_4Ni_3O_{10-\delta}$ and two its derivatives, $La_4Ni_{2.9}Cu_{0.1}O_{10-\delta}$ and $La_{3.95}Sr_{0.05}Ni_2CoO_{10-\delta}$, and one

* Corresponding author. Tel.: +351 234 370263; fax: +351 234 425300.
E-mail address: ayaremchenko@ua.pt (A.A. Yaremchenko).

0167-2738/$ – see front matter © 2009 Elsevier B.V. All rights reserved.
doi:10.1016/j.ssi.2009.02.022

Table 1
Crystal structure and average thermal expansion coefficients of cathode materials.

Cathode material	Synthesis of powders	Sintering of ceramics	Relative density, %	Crystal structure	Average TECs	
					T, K	$\bar{\alpha}\times10^6$, K^{-1}
$La_4Ni_3O_{10-\delta}$	1373 K/50 h	–	–	Orthorhombic $n=3$ RP ($Fmmm$)	548–1173	13.5 [14]
$La_4Ni_{2.9}Cu_{0.1}O_{10-\delta}$	1423 K/40 h	–	–	Orthorhombic $n=3$ RP ($Fmmm$)	–	–
$La_{3.95}Sr_{0.05}Ni_2CoO_{10-\delta}$	1423 K/10 h	–	–	Orthorhombic $n=3$ RP ($Fmmm$)	–	–
$La_2Ni_{0.5}Cu_{0.5}O_{4+\delta}$	1373 K/6 h	1553 K/5 h	91	Tetragonal $n=1$ RP ($I4/mmm$)	300–900	13.4
					900–1370	14.5
$Sr_{0.7}Ce_{0.3}Mn_{0.9}Cr_{0.1}O_{3-\delta}$	1423–1473 K/10 h	1713 K/5 h	94	Tetragonal perovskite ($I4/mcm$)	550–950	12.0
					950–1370	15.1
$SrMn_{0.6}Nb_{0.4}O_{3-\delta}$	1373–1473 K/20 h	1773 K/10 h	93	Rhombohedrally-distorted perovskite ($R3c$)	300–800	11.3
					800–1200	12.3
$Gd_{0.6}Ca_{0.4}Mn_{0.9}Ni_{0.1}O_{3-\delta}$	1473 K/5 h	1773 K/5 h	96	Orthorhombic perovskite ($Pbnm$)	550–900	10.8
					900–1370	12.1
$LaSr_2Mn_{1.6}Ni_{0.4}O_{7-\delta}$	1423–1593 K/40 h	1773 K/10 h	95	Tetragonal $n=2$ RP ($I4/mmm$)	300–900	12.5
					900–1370	14.4

mixed $n=2$ RP nickelate-manganite, $LaSr_2Mn_{1.6}Ni_{0.4}O_{7-\delta}$. For the latter materials, no information on the high-temperature electrical and electrochemical properties is found in the literature to date. Note also that the concentration of dopants (Cu, Sr and Ni) in the corresponding sublattices of $La_4Ni_{2.9}Cu_{0.1}O_{10-\delta}$, $La_{3.95}Sr_{0.05}Ni_2CoO_{10-\delta}$ and $LaSr_2Mn_{1.6}Ni_{0.4}O_{7-\delta}$, respectively, is close to the solubility limits; phase relationships in these oxide systems will be summarized in separate publications.

The present work is therefore focused on the comparative appraisal of cathodic performance of selected mixed-conducting phases in contact with $La_{10}Si_5AlO_{26.5}$ solid electrolyte [6] at 873–1073 K. Particular attention was also given to other properties important for the electrode applications, such as ionic and electronic transport, thermal expansion, and chemical compatibility of the cell components.

2. Experimental

Submicron $La_4Ni_3O_{10-\delta}$ powder used for the electrode preparation was synthesized via citrate-precursor route as reported elsewhere [20]. For the synthesis of other electrode materials, the glycine-nitrate process (GNP) was selected; GNP is well known as appropriate for multicomponent oxide systems where the use of a standard ceramic route may be hampered due to kinetics reason, and enables to prepare fine homogeneous powders with a large specific area [21]. The only exception relates to $SrMn_{0.6}Nb_{0.4}O_{3-\delta}$ synthesized by the standard solid-state reaction (SSR) method, since niobium nitrate necessary for the GNP does not exist. In all cases, the powders were annealed in air with several milling steps necessary to prepare single-phase materials; the powder firing conditions are listed in Table 1. For the studies of thermal expansion and transport properties of the electrode materials, gas-tight ceramic samples with density higher than 90% were compacted at 350–400 MPa and sintered in air (Table 1). Notice that, in the case of $n=3$ RP nickelates, sintering of gas-tight ceramics was impossible due to the RP phase decomposition at elevated temperatures, as discussed below. The $La_{10}Si_5AlO_{26.5}$ electrolyte supports with 93–94% density were prepared by SSR, with pre-reaction of the metal oxides at 1273–1473 K, pressing and sintering in air at 1923 K for 10 h; these preparation conditions were chosen on the basis of previous data [6].

The phase composition and crystal structure of electrode materials were studied by powder X-ray diffraction (XRD, Rigaku D/MAX-B diffractometer, CuK_a radiation). The thermal expansion in air was measured using a Linseis L75 alumina dilatometer in heating regime (3 K/min) at 298–1373 K. Thermogravimetric analysis (TGA, Setaram SetSys 16/18) was performed in a flow of dried air at heating and cooling rates of 2 K/min with isothermal equilibration steps. In order to determine the absolute oxygen content in RP nickelates, the samples were reduced to La_2O_3, SrO and metallic Ni, Co or Cu in a flow of dried 10%H_2–90%N_2 mixture at 1273–1373 K for 15 h. The total conductivity (σ) was measured by 4-probe DC method at 600–1300 K in air. The steady-state oxygen permeation fluxes (j) through dense ceramic membranes were determined as function of temperature and p(O_2) gradient using yttria-stabilized zirconia cells equipped with one oxygen pump and one sensor [22]; the measurements were performed at 973–1273 K, exposing feed-side surface of the membranes to atmospheric air.

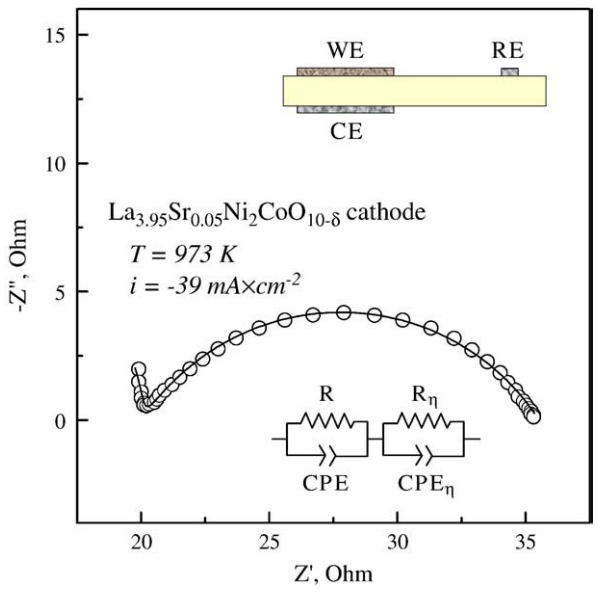

Fig. 1. Example of the impedance spectrum, analyzed using an equivalent circuit shown in the inset. Solid line corresponds to the fitting results. The upper inset illustrates the measuring cell configuration.

Table 2
Electrode fabrication conditions and polarization resistance of porous cathodes under open-circuit conditions in air.

Cathode	Electrode sintering	R_η, Ohm×cm^2		
		1073 K	973 K	873 K
$La_4Ni_3O_{10-\delta}$	1463 K/2 h	2.2	10.4	34
$La_4Ni_{2.9}Cu_{0.1}O_{10-\delta}$	1443 K/2 h	1.6	6.1	20
$La_{3.95}Sr_{0.05}Ni_2CoO_{10-\delta}$	1473 K/2 h	2.7	15	44
$La_2Ni_{0.5}Cu_{0.5}O_{4+\delta}$	1473 K/2 h	2.2	5.0	21
$La_2Ni_{0.8}Cu_{0.2}O_{4+\delta}$ [16]	1473 K/2 h	1.5	3.2	11.1
$Sr_{0.7}Ce_{0.3}Mn_{0.9}Cr_{0.1}O_{3-\delta}$	1503 K/2 h	10.2	23	–
$SrMn_{0.6}Nb_{0.4}O_{3-\delta}$	1473 K/2 h	31	–	–
$SrMn_{0.6}Nb_{0.4}O_{3-\delta}$ – PrO_x	–	5.4	41	–
$Gd_{0.6}Ca_{0.4}Mn_{0.9}Ni_{0.1}O_{3-\delta}$	1473 K/2 h	20	41	–
$LaSr_2Mn_{1.6}Ni_{0.4}O_{7-\delta}$	1503 K/2 h	24	54	–

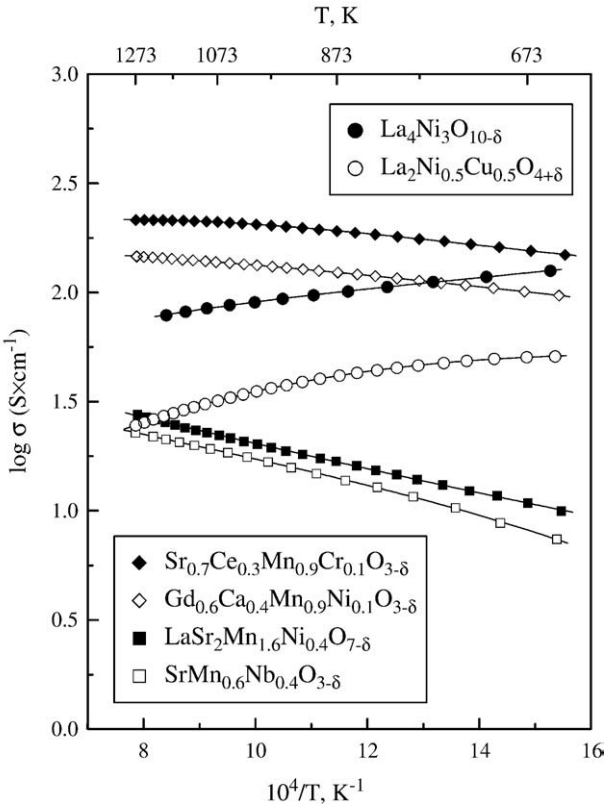

Fig. 2. Total conductivity of selected cathode materials in air. The data on $La_4Ni_3O_{10-\delta}$ with 58% density are taken from Ref. [14].

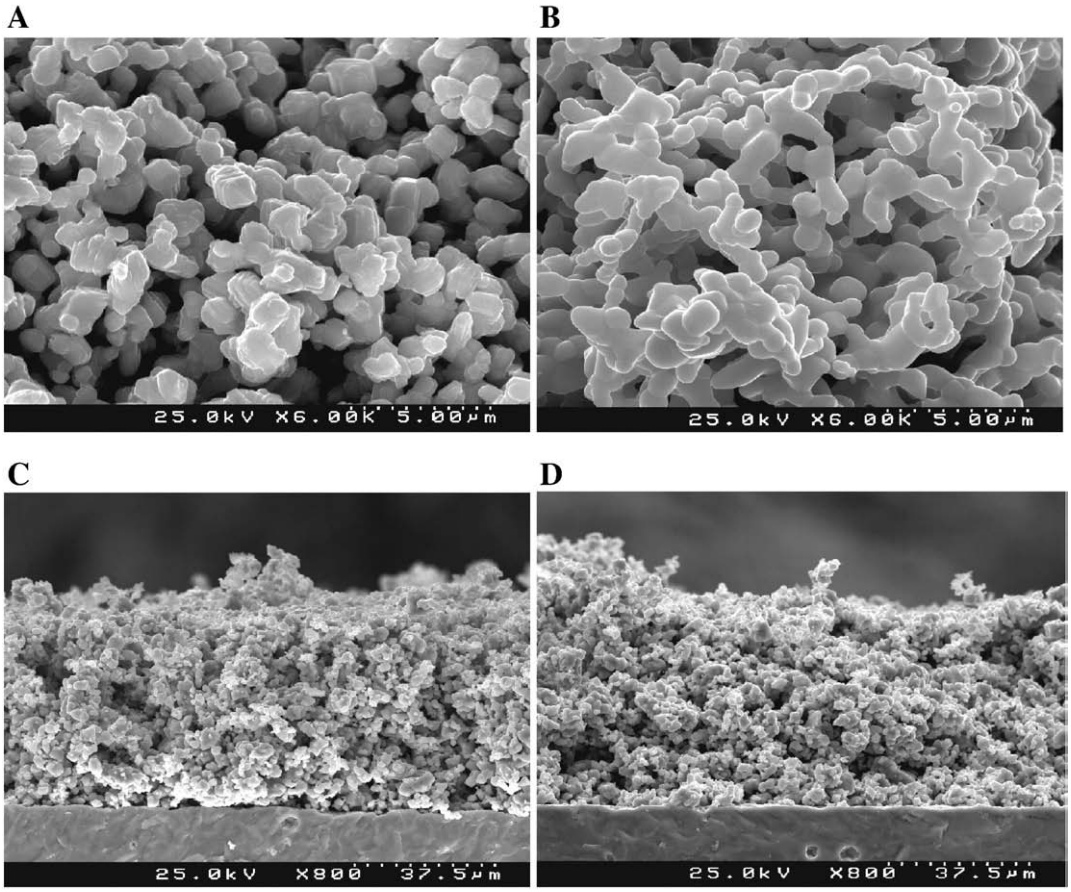

Fig. 3. SEM micrographs of as-prepared $La_4Ni_3O_{10-\delta}$ (A) and $Gd_{0.6}Ca_{0.4}Mn_{0.9}Ni_{0.1}O_{3-\delta}$ (B) cathode layers applied onto $La_{10}Si_5AlO_{26.5}$ solid electrolyte, and fractured $SrMn_{0.6}Nb_{0.4}O_{3-\delta}$ | $La_{10}Si_5AlO_{26.5}$ half-cells after fabrication (C) and after polarization tests (D).

The steady-state cathodic polarization was studied by the 3-electrode technique using the cells with symmetrical working and counter electrodes (WE and CE) and Pt mesh current collectors. The cell configuration (inset in Fig. 1) was chosen according to Ref. [23]. The porous WE layers were prepared by deposition of the electrode powders suspended in ethanol onto the dense $La_{10}Si_5AlO_{26.5}$ substrates, followed by final annealing in air (Table 2). The microstructure of electrodes was examined by scanning electron microscopy combined with energy-dispersive analysis (SEM/EDS, Hitachi S-4100 microscope, Rontec UHV detection system). The EDS spectra (analyzed area 1 μm^2; depth ~1 μm) were recorded on the fractured cell cross-sections, near the cathode/electrolyte interface (distance from the interface ~2 μm) and in the bulk of electrode and solid electrolyte. The counter and reference electrodes (CE and RE), both made of porous Pt, were sintered at 1273 K for 0.5 h. The experiments were performed in the galvanostatic mode using an AUTOLAB PGSTAT302 instrument at 873–1073 K in atmospheric air. The time necessary to attain steady-state conditions under DC polarization was 40–90 min. The ohmic (R) and polarization (R_η) resistances were extracted from the impedance spectra collected in the frequency range from 10 mHz to 1 MHz. One typical spectrum is presented in Fig. 1; the fitting results to an equivalent circuit (inset) are shown as solid line. The statistical errors for the calculated polarization resistance did not exceed ±2%. Selected electrodes were surface-modified with PrO_x via impregnation with a saturated ethanol solution of $Pr(NO_3)_3$*$5H_2O$, subsequent drying, and annealing at 1073 K. For the sake of comparison, several electrode materials were also evaluated in contact with $(La_{0.9}Sr_{0.1})_{0.98}Ga_{0.8}Mg_{0.2}O_{3-\delta}$ (LSGM) electrolyte [24]. Chemical interaction between the solid-electrolyte and electrode compositions was assessed annealing mixtures of these materials (50:50 wt.%) at the electrode fabrication temperature and with subsequent XRD analysis.

3. Results and discussion

3.1. Characterization of electrode materials

XRD analysis showed that for all dense ceramics and for all electrode powders, both as-prepared and annealed under the electrode fabrication conditions, single perovskite-related phases are formed. No traces of secondary phases were observed. The crystal structures were identified as tetragonal K_2NiF_4-type for $La_2Ni_{0.5}Cu_{0.5}O_{4+\delta}$, tetragonal $Sr_3Ti_2O_7$-type for $LaSr_2Mn_{1.6}Ni_{0.4}O_{7-\delta}$, orthorhombic Ruddlesden–Popper ($n=3$) for all $La_4Ni_3O_{10}$-based compositions, and perovskite-type with different lattice distortions for the doped manganites (Table 1). The results are in agreement with literature data (Refs. [14,25,26], and PDF cards no. 83–1164, 80–1075 and 86–0494).

For most studied materials, the average thermal expansion coefficients (TECs, $\bar{\alpha}$) tend to increase with temperature (Table 1). This trend is primarily associated with oxygen release on heating and the corresponding reduction of transition metal cations, increasing their radii (e.g. [9]). Nevertheless, all TECs in the intermediate temperature range (Table 1) are still compatible with that of $La_{10}Si_5AlO_{26.5}$ solid electrolyte where $\bar{\alpha}=9.1\times10^{-6}$ K^{-1} at 473–1173 K [6].

The temperature dependence of total conductivity of the prepared electrode materials in air is displayed in Fig. 2. Numerous literature data (e.g. Refs. [9,12,17,18,27] and references therein) show that the conductivity of manganite- and nickelate-based compositions is predominantly electronic. For instance, the oxygen-ionic transport in La_2NiO_4-based materials is reported to be 10^2–10^4 times lower compared to the electronic conduction at 973–1273 K [17,28]. For $Sr_{0.7}Ce_{0.3}Mn_{0.9}Cr_{0.1}O_{3-\delta}$ and $LaSr_2Mn_{1.6}Ni_{0.4}O_{7-\delta}$ studied in the

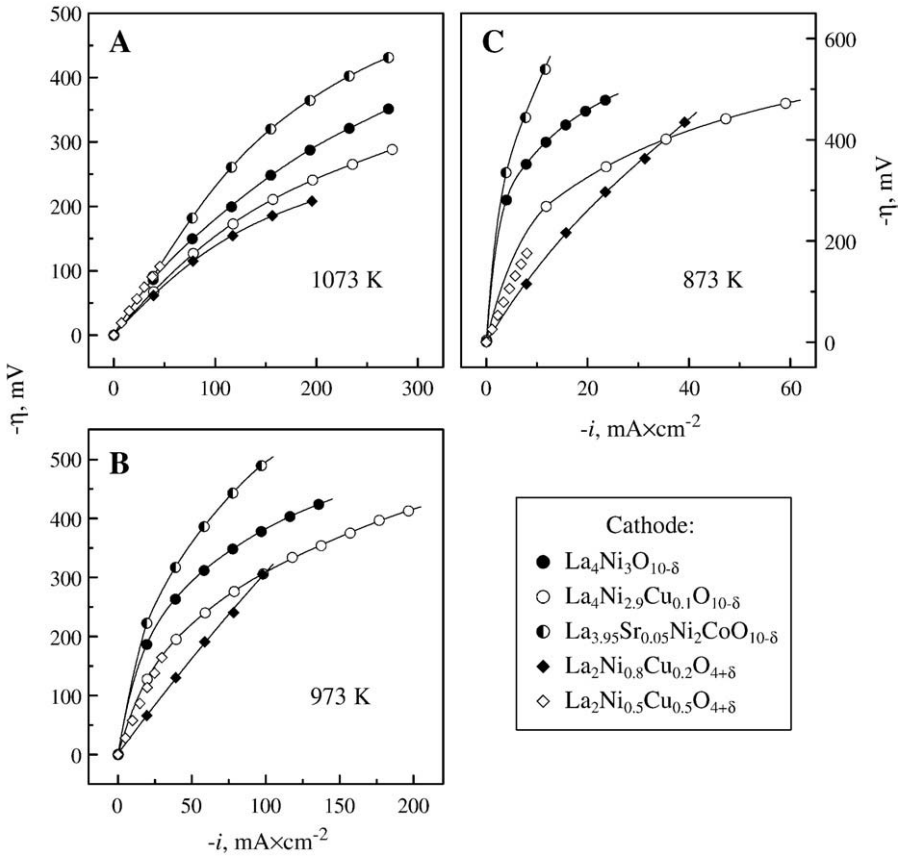

Fig. 4. Cathodic overpotentials of porous nickelate electrodes in contact with $La_{10}Si_5AlO_{26.5}$ electrolyte in air. The data on $La_2Ni_{0.8}Cu_{0.2}O_{4+\delta}$ cathode [16] are shown for comparison.

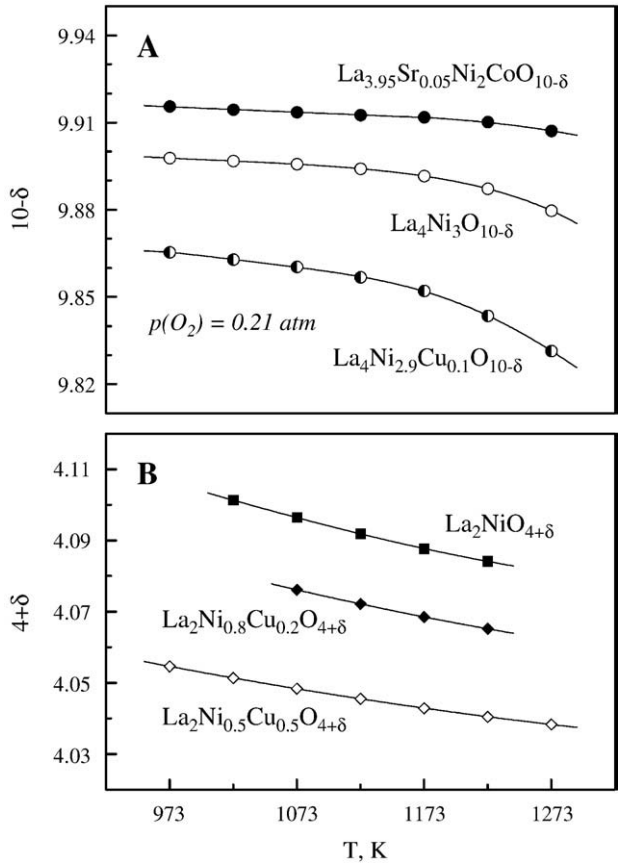

Fig. 5. Temperature dependence of the oxygen nonstoichiometry of the $n=3$ (A) and $n=1$ (B) RP nickelates at atmospheric oxygen pressure. The data on $La_2NiO_{4+\delta}$ and $La_2Ni_{0.8}Cu_{0.2}O_{4+\delta}$ are taken from [27].

present work, the ionic contribution to the total conductivity was estimated from the oxygen permeation data discussed below, and is lower than 0.003% at 1298 K and further decreases on cooling. The electronic transport in both manganite and nikelate phases is considered to occur via the small-polaron conduction mechanism [9,12,17,28]. However, whilst the conductivity in Mn-containing ceramics is temperature-activated, nikelate phases exhibit a pseudo-metallic behavior (Fig. 2). The latter phenomenon originates from the oxygen losses when temperature increases, resulting in decreasing electronic charge-carrier concentration [17,18,27,28]. This conclusion was confirmed by TGA. Regardless of the microscopic mechanisms, at 873–1073 K the total conductivity varies in the range from 190–210 S/cm for $Sr_{0.7}Ce_{0.3}Mn_{0.9}Cr_{0.1}O_{3-\delta}$ down to 14–22 S/cm for $LaSr_2Mn_{1.6}Ni_{0.4}O_{7-\delta}$ and $SrMn_{0.6}Nb_{0.4}O_{3-\delta}$.

One should also mention that sintering of dense $La_4Ni_3O_{10-\delta}$-based ceramics was impossible due to thermodynamic instability of these phases at elevated temperatures. XRD and TGA demonstrated that at atmospheric oxygen pressure, the thermal decomposition of $La_4Ni_3O_{10-\delta}$, $La_4Ni_{2.9}Cu_{0.1}O_{10-\delta}$ and $La_{3.95}Sr_{0.05}Ni_2CoO_{10-\delta}$ and the separation of La_2NiO_4-based solid solutions with K_2NiF_4-type structure occur at approximately 1480 K, 1460 K and 1530–1570 K, respectively. The conductivity of $La_4Ni_3O_{10-\delta}$ shown in Fig. 2 corresponds to a highly-porous sample sintered at 1323 K (58% density [14]) and is, therefore, significantly undervalued.

3.2. Sintering and microstructure of porous cathodes

All porous electrode layers studied in contact with $La_{10}Si_5AlO_{26.5}$ solid electrolyte were fabricated under similar conditions, with annealing at temperatures close to 1473 K for 2 h, in air (Table 2). The sintering temperature was slightly lower for $La_4Ni_3O_{10-\delta}$ and $La_4Ni_{2.9}Cu_{0.1}O_{10-\delta}$ cathodes in order to prevent the phase decomposition. For $Sr_{0.7}Ce_{0.3}Mn_{0.9}Cr_{0.1}O_{3-\delta}$ and $LaSr_2Mn_{1.6}Ni_{0.4}O_{7-\delta}$, the sintering temperature was lifted up to 1503 K in order to achieve necessary adhesion and mechanical strength of the porous electrodes.

Typical microstructures of as-prepared cathodes are shown in Fig. 3(A–C). The electrodes are characterized with uniform grain distribution and the grain size of 0.5–3.0 μm. The thickness of porous layers varied in the range 20–40 μm; the sheet density and estimated porosity were 13 ± 3 mg/cm^2 and ~40%, respectively. No substantial sintering was revealed by SEM after the polarization experiments; as an example, Fig. 3(C and D) compares the microstructures of $SrMn_{0.6}Nb_{0.4}O_{3-\delta}$ cathode before and after testing.

3.3. Electrochemical performance of nickelate-based cathodes

Fig. 4 presents the cathodic current–overpotential curves of nickelate-based electrodes at atmospheric oxygen pressure; the values of their polarization resistance under open-circuit conditions are listed in Table 2. No tendencies to limiting currents were observed. For $n=3$ RP nickelates, the electrochemical activity increases in the sequence $La_{3.95}Sr_{0.05}Ni_2CoO_{10-\delta}<La_4Ni_3O_{10-\delta}<La_4Ni_{2.9}Cu_{0.1}O_{10-\delta}$, correlating with the oxygen nonstoichiometry (Fig. 5A). Since the concentration of interstitial anions in the rock-salt type layers of oxygen-deficient $n=3$ RP nickelates is negligibly low, the observed correlation might indicate a key role of bulk ionic conductivity dominated by the vacancy diffusion in perovskite layers of the RP lattices. Indeed, qualitatively similar relationships between the oxygen excess (Fig. 5B), ionic transport and cathodic polarization (Fig. 4 and Table 2) can be revealed for oxygen-hyperstoichiometric $La_2(Ni,Cu)O_{4+\delta}$ with K_2NiF_4-type structure, where the ionic conduction is essentially governed by the interstitial anion migration [14–18].

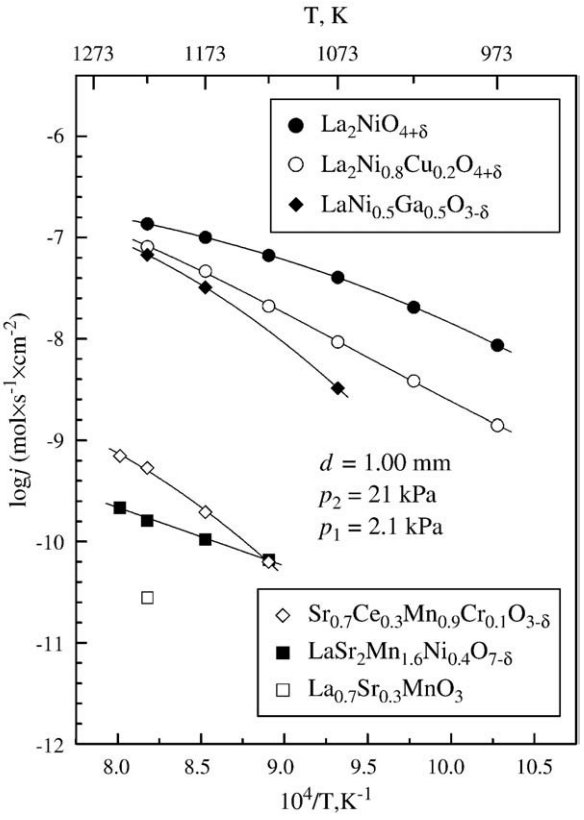

Fig. 6. Comparison of the oxygen permeation fluxes through dense nickelate- and manganite-based ceramic membranes under fixed oxygen partial pressure gradient. d is the membrane thickness; p_2 and p_1 correspond to oxygen partial pressure at the feed and permeate sides, respectively. The literature data are taken from Ref. [17,22,29].

Table 3
Comparison of the polarization resistance of nickelate-based cathodes in contact with various solid electrolytes under open circuit conditions in air.

Cathode	Electrolyte	R_η, Ohm × cm^2		Ref.
		1073 K	973 K	
$La_2Ni_{0.5}Cu_{0.5}O_{4+\delta}$	$La_{10}Si_5AlO_{26.5}$	2.2	–	This work
	$(La_{0.9}Sr_{0.1})_{0.98}Ga_{0.8}Mg_{0.2}O_{3-\delta}$	1.6	–	This work
$La_2Ni_{0.8}Cu_{0.2}O_{4+\delta}$	$La_{10}Si_5AlO_{26.5}$	1.5	3.2	[16]
	$(La_{0.9}Sr_{0.1})_{0.98}Ga_{0.8}Mg_{0.2}O_{3-\delta}$	0.6	2.0	[16]
	$(ZrO_2)_{0.92}(Y_2O_3)_{0.08}$	6.1	28	[19]
$La_4Ni_3O_{10-\delta}$	$La_{10}Si_5AlO_{26.5}$	2.2	10.4	This work
	$La_{0.9}Sr_{0.1}Ga_{0.8}Mg_{0.2}O_{3-\delta}$	0.9	5.1	[14]

The substitution of copper for nickel in $La_2Ni_{1-x}Cu_xO_{4+\delta}$ leads to a lower concentration of extra oxygen and has negative impact on the ion diffusivity and oxygen permeability (Fig. 6 and Refs. [18,27]). These trends all suggest that the concentration of mobile ionic charge carriers and bulk ionic transport significantly affect the oxygen reduction kinetics on the RP nickelate cathodes. Analogous correlations between the ion diffusion, electrode material surface exchange and electrochemical activity are often observed for mixed-conducting electrodes due to expansion of the electrochemical reaction zone along the electrode/gas and electrode/electrolyte interfaces. Although the substitution of nickel in $La_2Ni_{1-x}Cu_xO_{4+\delta}$ and $La_4Ni_{3-x}Co_xO_{10-\delta}$ series decreases also their electronic conductivity [15,18], any significant influence of the latter factor on nickelate cathodes performance seems unlikely.

At the same time, the overpotentials of RP nickelate electrodes applied onto $La_{10}Si_5AlO_{26.5}$ electrolyte are higher than those in contact with LSGM (Table 3). In addition to the transport properties and exchange currents of solid-electrolyte ceramics, this difference may be contributed by chemical interaction between the electrode and electrolyte materials. Although no secondary phases were revealed by XRD in the electrode/electrolyte powder mixtures annealed under electrode fabrication conditions (Fig. 7, A–C), EDS inspection of the electrochemical cells detected a presence of SiO_2 on the electrode grains near the electrode/electrolyte interface; one example is shown in Fig. 8A. The minor silica diffusion along the cathode surface may result in partial blocking of the electrochemical reaction zone. It should be mentioned that substantially larger polarization resistances were reported for $La_2Ni_{0.8}Cu_{0.2}O_{4+\delta}$ cathode in contact with yttria-stabilized zirconia electrolyte (Table 3), when the relatively poor performance is caused by chemical interaction between the electrode and electrolyte materials [19]. This topotactic reaction leading to the formation of insulating $La_2Zr_2O_7$ phase at the interface, is well known for the LSM cathodes [9].

3.4. Behavior of manganite-based electrodes

The performance of manganite-based cathodes in contact with $La_{10}Si_5AlO_{26.5}$ is substantially worse compared to nickelates (Figs. 4

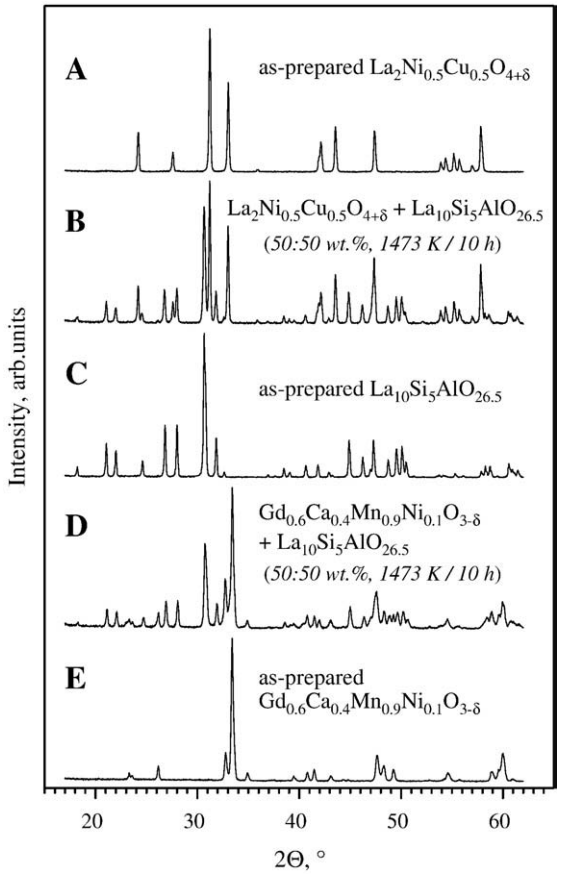

Fig. 7. XRD patterns of as-prepared electrode materials (A and E), as-prepared $La_{10}Si_5AlO_{26.5}$ solid electrolyte (C), and electrode/electrolyte powder mixtures annealed at 1473 K for 10 h (B and D).

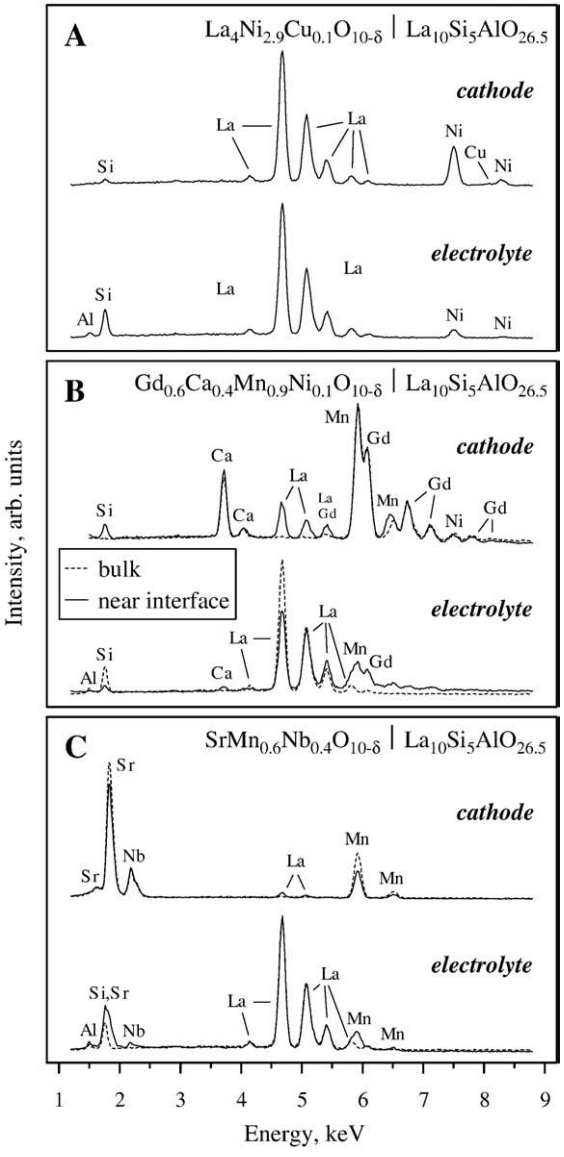

Fig. 8. Comparison of the EDS spectra of electrode grains in the porous electrode bulk and near electrode/electrolyte interface, and $La_{10}Si_5AlO_{26.5}$ in the electrolyte bulk and near the interface.

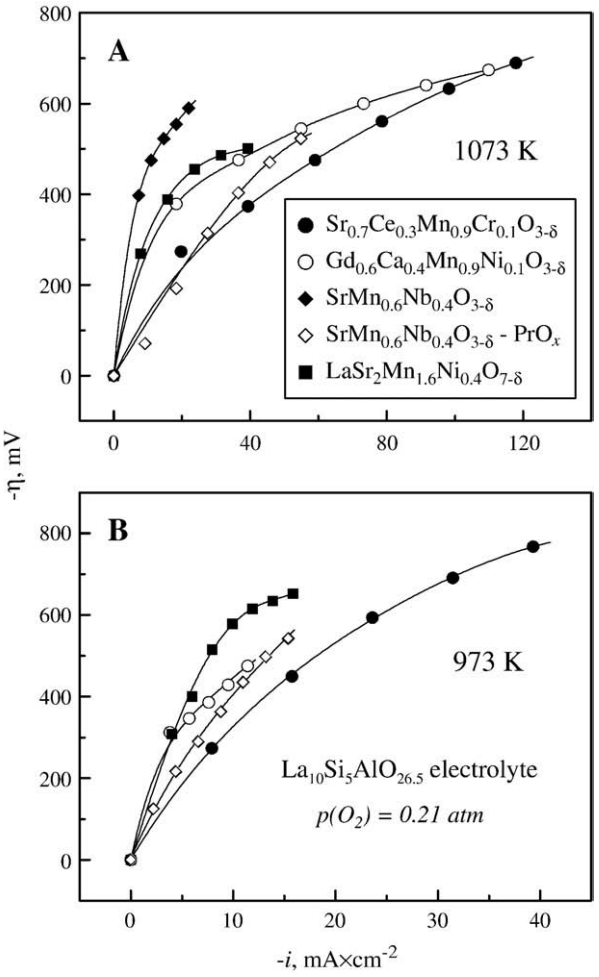

Fig. 9. Cathodic overpotentials of porous manganite electrodes in contact with $La_{10}Si_5AlO_{26.5}$ electrolyte at 1073 K (A) and 973 K (B) in air.

and 9, Table 2). This correlates, again, with much lower level of the ionic transport typical for manganites (Fig. 6). At 1073 K and cathodic currents of 40–120 mA/cm^2, the overpotentials of $Sr_{0.7}Ce_{0.3}Mn_{0.9}Cr_{0.1}O_{3-\delta}$, $Gd_{0.6}Ca_{0.4}Mn_{0.9}Ni_{0.1}O_{3-\delta}$ and $LaSr_2Mn_{1.6}Ni_{0.4}O_{7-\delta}$ electrodes are 4–8 time higher than those of porous nickelate layers. The worst performance is observed for $SrMn_{0.6}Nb_{0.4}O_{3-\delta}$ | $La_{10}Si_5AlO_{26.5}$ half-cells, where poor electrochemical activity is partly associated with relatively low electronic conductivity of $SrMn_{0.6}Nb_{0.4}O_{3-\delta}$ (Fig. 2). As expected, the infiltration of PrO_x into porous $SrMn_{0.6}Nb_{0.4}O_{3-\delta}$ matrix reduces polarization (Table 2 and Fig. 9); such an improvement may originate from numerous factors, including enhanced surface exchange for both electrolyte and electrode, enlargement of the triple-phase boundary and electrode surface area, and even improved electronic transport along the electrode [9]. The impact of surface moditification is, however, rather insufficient in the present case; the cathodic overpotential of $SrMn_{0.6}Nb_{0.4}O_{3-\delta}$-$PrO_x$ | $La_{10}Si_5AlO_{26.5}$ half-cells is still as high as −500 mV at 1073 K and −50 mA/cm^2.

As for the nickelate-based cathodes, the poor performance of manganite electrodes applied onto silicate solid electrolyte is contributed by the surface diffusion of SiO_2. Whilst identification of SiO_2 traces is complicated for strontium-containing electrodes due to overlapping of Sr and Si peaks in the EDS spectra, the presence of silica was clearly detected on the surface of $Gd_{0.6}Ca_{0.4}Mn_{0.9}Ni_{0.1}O_{3-\delta}$ cathode near the interface (Fig. 8B). In addition, EDS analysis of the electrolyte/electrode interfaces indicated a critical role of cation interdiffusion between the manganite electrodes and $La_{10}Si_5AlO_{26.5}$ Fig. 8(B and C) presents two typical examples of EDS spectra displaying, in particular, significant penetration of alkaline-earth and manganese cations into the surface layers of $La_{10}Si_5AlO_{26.5}$, accompanied with the corresponding compositional changes in the electrode layers near interface. The interdiffusion seems to occur faster compared to nickelates. On the other hand, XRD inspections of the manganite/$La_{10}Si_5AlO_{26.5}$ powder mixtures did not reveal any substantial amount of impurity phases (Fig. 7, C–E). This indicates that the reaction depth is essentially limited, whereas the cation interdiffusion results primarily in the compositional changes within the reacting phases and in the segregation of small amounts of amorphous phases at the interface and grain boundaries. In any case, significant compositional alterations near the electrode/electrolyte interface should induce partial decomposition of perovskite-type phases and formation of thin insulating interlayers. Furthermore, the introduction of Sr^{2+} or Ca^{2+} in the La^{3+} sites of apatite-type silicates decreases their ionic conductivity [5]; a similar effect is observed on Mn doping [2]. As a general rule, the electrode polarization resistance increases with solid-electrolyte resistivity [7,30].

4. Conclusions

The cathodic performance of a series of perovskite-related nickelates and manganites, having moderate thermal expansion compatible with that of lanthanum silicate-based solid electrolytes, was evaluated in contact with apatite-type $La_{10}Si_5AlO_{26.5}$ electrolyte at 873–1073 K and atmospheric oxygen pressure. The electrochemical activity of $La_{n+1}Ni_nO_{3n+1}$-based compositions exhibit a correlation with the concentration of mobile oxygen defects and bulk ionic conductivity, thus decreasing in the sequence $La_4Ni_{2.9}Cu_{0.1}O_{10-\delta}$ > $La_4Ni_3O_{10-\delta}$ > $La_{3.95}Sr_{0.05}Ni_2CoO_{10-\delta}$. A similar decrease is observed on copper doping in K_2NiF_4-type $La_2Ni_{1-x}Cu_xO_{4-\delta}$. Whilst the performance of nickelate-based cathodes may be further improved using appropriate doping and microstructural engineering approaches, thorough optimization of the electrode fabrication conditions is also required in order to suppress SiO_2 diffusion from the electrolyte surface. As compared to the RP nickelate derivatives, the manganite-based porous layers exhibit relatively poor electrochemical properties determined by the lower level of oxygen-ionic conduction and strong cation interdiffusion between the electrode and electrolyte materials.

Acknowledgements

This work was supported by the FCT, Portugal (project PTDC/CTM/64357/2006), and the MatSILC project (STRP 033410, CEC). Experimental assistance and helpful discussions made by A. Shaula, E. Tsipis, A. Kovalevsky and Y. Pivak, are gratefully acknowledged.

References

[1] S. Nakayama, T. Kageyama, H. Aono, Y. Sadaoka, J. Mater. Chem. 5 (1995) 1801.
[2] J. McFarlane, S. Barth, M. Swaffer, J.E.H. Sansom, P.R. Slater, Ionics 8 (2002) 149.
[3] P.J. Panteix, I. Julien, P. Abelard, D. Bernache-Assollant, J. Eur. Ceram. Soc. 28 (2008) 821.
[4] A. Brisse, A.-L. Sauvet, C. Barthet, S. Georges, J. Fouletier, Solid State Ionics 178 (2007) 1337.
[5] V.V. Kharton, F.M.B. Marques, A. Atkinson, Solid State Ionics 174 (2004) 135.
[6] A.L. Shaula, V.V. Kharton, F.M.B. Marques, J. Solid State Chem. 178 (2005) 2050.
[7] E.V. Tsipis, V.V. Kharton, J. Solid State Electrochem. 12 (2008) 1039.
[8] D.J.L. Brett, A. Atkinson, N.P. Brandon, S.J. Skinner, Chem. Soc. Rev. 37 (2008) 1568.
[9] E.V. Tsipis, V.V. Kharton, J. Solid State Electrochem. 12 (2008) 1367.
[10] Y. Sakaki, Y. Takeda, A. Kato, N. Imanishi, O. Yamamoto, M. Hattori, M. Iio, Y. Esaki, Solid State Ionics 118 (1999) 187.
[11] S. Hashimoto, H. Iwahara, Mater. Res. Bull. 35 (2000) 2253.
[12] I.P. Marozau, V.V. Kharton, A.P. Viskup, J.R. Frade, V.V. Samakhval, J. Eur. Ceram. Soc. 26 (2006) 1371.
[13] S. Tao, J.T.S. Irvine, J. Mater. Chem. 12 (2002) 2356.
[14] G. Amow, I.J. Davidson, S.J. Skinner, Solid State Ionics 177 (2006) 1205.
[15] G. Amow, J. Au, I. Davidson, Solid State Ionics 177 (2006) 1837.
[16] E.V. Tsipis, V.V. Kharton, J.R. Frade, Electrochim. Acta 52 (2007) 4428.

[17] V.V. Kharton, E.V. Tsipis, A.A. Yaremchenko, J.R. Frade, Solid State Ionics 166 (2004) 327.
[18] E. Boehm, J.M. Bassat, M.C. Steil, P. Dordor, F. Mauvy, J.C. Grenier, Solid State Sci. 5 (2003) 973.
[19] A. Aguadero, J.A. Alonso, M.J. Escudero, L. Daza, Solid State Ionics 179 (2008) 393.
[20] D.O. Bannikov, V.A. Cherepanov, J. Solid State Chem. 179 (2006) 2721.
[21] L.A. Chick, L.R. Pederson, G.D. Maupin, J.L. Bates, L.E. Thomas, G.L. Exarhos, Mater. Lett. 10 (1990) 6.
[22] A.A. Yaremchenko, V.V. Kharton, A.P. Viskup, E.N. Naumovich, N.M. Lapchuk, V.N. Tikhonovich, J. Solid State Chem. 142 (1999) 325.
[23] J. Mizusaki, H. Tagawa, K. Isobe, M. Tajika, I. Koshiro, H. Maruyama, K. Hirano, J. Electrochem. Soc. 141 (1994) 1674.
[24] V.V. Kharton, A.L. Shaula, N.P. Vyshatko, F.M.B. Marques, Electrochim. Acta 48 (2003) 1817.
[25] A. Sundaresan, J.L. Tholence, A. Maignan, C. Martin, M. Hervieu, B. Raveau, E. Suard, Eur. Phys. J., B 14 (2000) 431.
[26] O. Peña, M. Bahout, K. Ghanimi, P. Duran, D. Gutierre, C. Moure, J. Mater. Chem. 12 (2002) 2480.
[27] E.N. Naumovich, M.V. Patrakeev, V.V. Kharton, A.A. Yaremchenko, D.I. Logvinovich, F.M.B. Marques, Solid State Sci. 7 (2005) 1353.
[28] A.A. Yaremchenko, V.V. Kharton, M.V. Patrakeev, J.R. Frade, J. Mater. Chem. 13 (2003) 1136.
[29] V.V. Kharton, A.V. Kovalevsky, M. Avdeev, E.V. Tsipis, M.V. Patrakeev, A.A. Yaremchenko, E.N. Naumovich, J.R. Frade, Chem. Mater. 19 (2007) 2027.
[30] T. Kenjo, Y. Kanehira, Solid State Ionics 148 (2002) 1.